Acta Mech
https://doi.org/10.1007/s00707-024-04083-x

ORIGINAL PAPER

Shihao Lv · Bingyang Li · Yan Shi · Cunfa Gao

Phase field fracture modelling of flexible piezoelectric materials considering different electrical boundary conditions

Received: 24 April 2024 / Revised: 12 July 2024 / Accepted: 24 August 2024

Abstract Flexible piezoelectric materials have gained considerable attention due to their remarkable properties, including electromechanical coupling and high stretchability. These characteristics make them valuable in the realm of flexible electronic devices. However, the issue of fracture in these materials cannot be ignored. In general, these flexible/stretchable materials experience fractures when subjected to significant deformation, unlike brittle piezoelectric materials with low failure strain which have been extensively studied. There is a pressing need to investigate the fracture behavior of flexible piezoelectrics under finite deformation conditions. Within the framework of the phase field method, this work addresses the fracture of flexible piezoelectrics utilizing a nonlinear electromechanical material model. To investigate the influence of electrical boundary conditions on fracture behavior, a function related to the electric permittivity ratio and phase field variable is employed to degrade the electric energy density. By adjusting the electric permittivity ratio, the analysis encompasses the fracture behavior of flexible piezoelectric materials under the assumptions of electrically impermeable, semi-permeable, and permeable conditions, respectively. In order to solve the coupled governing equations, a residual controlled staggered algorithm (RCSA) is employed in the user element subroutine of commercial software ABAQUS. The simulation results indicate that fracture behavior in flexible piezoelectric materials is influenced by several factors, including material parameters, geometry, polarization direction, and the external electric field. Notably, when the poling direction is perpendicular to the electric field direction, variations in the external electric field have a minimal impact on fracture behavior. In contrast, when the poling direction is parallel to the electric field direction, the influence on fracture behavior is pronounced. These findings provide valuable insights for developing strategies to enhance the fracture resistance and durability of flexible piezoelectric materials in practical applications.

Abbreviations

B_r	Reference configuration
∂B_r	External boundary
B_r^e	Discrete undeformable body
B_t	Deformed configuration
B_t^e	Discrete deformable body
Γ	Sharp crack surface
$\mathbf{F}$	Deformation gradient

S. Lv · Y. Shi (✉) · C. Gao
State Key Laboratory of Mechanics and Control for Aerospace Structures, Nanjing University of Aeronautics and Astronautics, Nanjing 210016, China
e-mail: yshi@nuaa.edu.cn

B. Li
China Academy of Aerospace Science and Innovation, Beijing 100871, China

Published online: 04 September 2024

$\boldsymbol{\gamma}$	Green-Lagrange strain
$\mathbf{I}$	Identity tensor
α	Phase field variable
α_n	Converged phase field variable at the previous increment
Γ_{l_0}	Diffuse crack surface
G_c	Critical energy release rate
η	Viscous parameter
t	Time
τ	Time-like scalar variable
ψ_{em}	Mixed energy-enthalpy per unit volume
ψ_m	Mechanical energy density
ψ_c	Coupled energy density
ψ_e	Electric energy density
ψ_v	Mechanical energy density
ψ_v^+	Positive part of mechanical energy density
ψ_v^-	Negative part of mechanical energy density
g_m, g_c, and g_e	Degradation function
ϵ_c	Electric permittivity of crack
ϵ_p	Electric permittivity of piezoelectric material
ζ	A variable defining electrical boundary conditions
$\mathbf{t}$	Prescribed surface traction force
w	Prescribed surface free charge density
$S_{\mathbf{t}}$	External boundary with surface force
S_w	External boundary with surface free charge density
k	An artificial parameter with a small value
$\tilde{\mathrm{E}}$	Referential electric field intensity
$\mathbf{E}$	Spatial electric field intensity
$\tilde{D}_i$	Referential electric displacement
D_i	Spatial electric displacement
ϕ, and ϕ^*	Electric potential
S_{ij}	The first Piola–Kirchhoff stress
σ_{ij}	Cauchy stress
μ	Initial shear modulus
K_0	Initial bulk modulus
ϵ_{ij}	Dielectric tensor
e_{ijk}	Piezoelectric tensor
J	Volume variation
W_{int}	Internal energy
W_{ext}	External energy
$\overline{I}_1$	The first invariant of the distortional right Cauchy-Green deformation tensor
N^A	Shape function
$R^A_{u_i}$, R^A_ϕ, and R^A_α	Residual vectors
$K_{u_i^A u_k^B}$, $K_{u_i^A \phi^B}$, $K_{\phi^A u_i^B}$, $K_{\phi^A \phi^B}$, and $K_{\alpha^A \alpha^B}$	Stiffness matrices
$\mathbf{n}$	Unit outward-pointing normal vector
l_0	Length scale parameter for the phase field
$\boldsymbol{P}$	Poling direction
γ_a	Eigenvalue of the strain
n_a	Eigenvector of the strain
$\mathcal{H}$	History field
L, w, and h	Length, width, and height of piezoelectric specimen
$\mathbf{u}$	Displacement
Δu	Displacement increment

1 Introduction

Flexible piezoelectric materials have attracted considerable attention due to their exceptional properties, characterized by high stretchability and electromechanical coupling [1]. These materials hold immense promise for applications in flexible electronics, such as wearable devices and foldable displays [2, 3], biomedical sensors for health monitoring [4, 5], and energy harvesting from ambient mechanical vibrations [2]. The development of flexible piezoelectric materials with superior tensile properties and durability has been a primary focus of numerous experimental studies [6, 7].

Polyvinylidene fluoride (PVDF) has emerged as a highly promising material for flexible piezoelectric applications [7, 8]. Experimental studies have demonstrated that PVDF-based stretchable soft materials exhibit a notable stress-softening phenomenon [8]. To elucidate the nonlinear behavior of flexible piezoelectric materials, Lv et al. [9] proposed a nonlinear electromechanical model based on the Neo-Hookean material model and electromechanical theory. This model provides valuable insights into the electromechanical coupling and nonlinear mechanical response exhibited by these materials. Nevertheless, further investigation is still required to explore the fracture behavior of these materials.

Fracture failure of piezoelectric materials has become a significant concern in engineering fields [10–12]. The fracture behavior of these materials plays a critical role in determining the performance and reliability of related devices. However, previous investigations have predominantly focused on brittle piezoelectric materials under the assumption of small deformations. While this approximation is suitable for materials like Lead Zirconate Titanate (PZT) [2] and Barium Titanate ($BaTiO_3$) [13], it may not adequately capture the behavior of flexible piezoelectrics. In general, flexible piezoelectrics exhibit considerable failure strain and undergo finite deformation upon fracture.

Electromechanical fracture in piezoelectric solids requires careful consideration of the electrical boundary conditions at crack surfaces [12]. These conditions are contingent upon the medium present within the crack [14], typically classified as permeable, semi-permeable, and impermeable [12, 14]. In a permeable boundary condition [15], both the electric potential and the normal component of electric displacement are assumed to be continuous across the crack surfaces, ensuring no disruption in electrical properties at the interface. Conversely, the impermeable case [16] assumes that the medium inside the crack has no conductivity and prohibits the passage of electric current. In this case, the normal component of electric displacement is considered to be zero at the top and bottom surfaces of the crack. The semi-permeable assumption [17] posits that the filling medium within the crack can sustain a certain level of electric field, thereby inducing electric displacement. These distinct electrical boundary conditions along the crack surfaces may influence fracture behavior. In the simulation process, it is crucial to choose appropriate electrical boundary conditions to accurately assess the reliability of these materials. In the framework of small deformation, several studies [18, 19] have investigated the effect of electrical boundary conditions on brittle piezoelectric materials. However, the influence of these boundary conditions on flexible piezoelectric materials has not been thoroughly explored.

Within the framework of finite deformation, there have been several studies investigating fracture problems utilizing the phase field method. Tang et al. [20] proposed an energy decomposition approach to simulate the fracture behavior of nonlinearly elastic materials. Arash et al. [21] developed a finite deformation phase field model to investigate the thermo-viscoelastic fracture behavior and predict failure processes in polymer nanocomposites. Zuo and Zhao [22] established a model incorporating finite deformation, elastic softening, and plastic flow to analyze the stress evolution of spherical silicon particles. These investigations demonstrate the effectiveness of the phase-field method in simulating finite deformation fracture phenomena in flexible materials. Nonetheless, there remains a scarcity of dedicated studies on phase field models specifically addressing electromechanical fracture in flexible piezoelectric materials.

Numerical simulation plays a crucial role in studying the fracture characteristics of piezoelectric materials, allowing visualization of stress and electric field distribution during the loading process. This enables a deeper understanding of the fracture behavior of the material. Various numerical methods are employed to address fracture problems [23–25], such as singular element [26], cohesive zone [12], extended finite element [13], and phase field [14, 27, 28] methods. Among these, the phase field method has proven particularly effective. It transforms the challenge of crack propagation and evolution into an energy minimization problem involving multiple coupled fields. This transformation allows for direct solutions to complex fracture problems, providing a powerful tool for studying electromechanical fracture in piezoelectric materials. In solving phase field fracture problems, both monolithic and staggered procedures are commonly utilized. The staggered scheme is notable for its robustness: it sequentially handles variables as staggered fields and solves them independently [29].

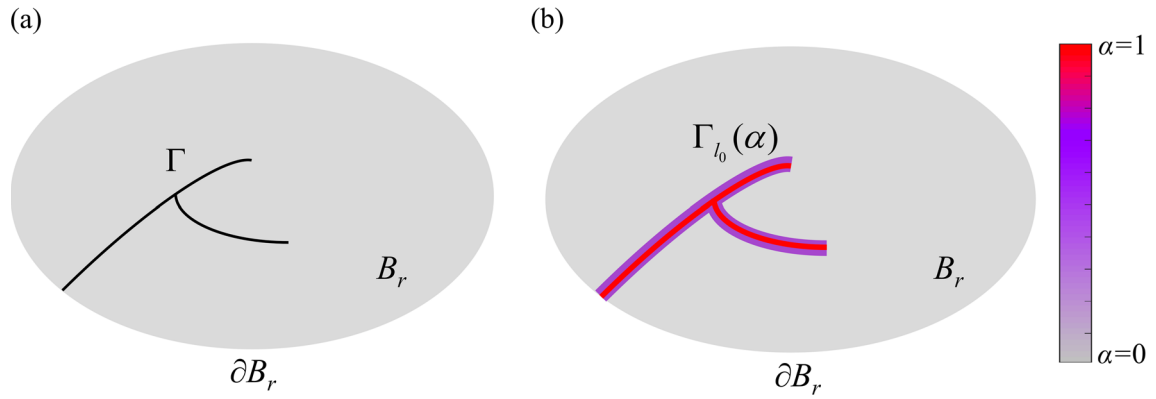

Fig. 1 Schematic representation of a two-dimensional piezoelectric solid with the presence of **a** a sharp crack and **b** a diffuse crack $\Gamma_{l_0}(\alpha)$ approximated using the phase field variable α

This approach simplifies the solution process and enhances computational efficiency, making it a preferred choice in many phase field simulations of fracture.

According to Griffith's theory, crack propagation occurs when the energy release rate surpasses a critical threshold. Francfort and Marigo [30] extended Griffith's theory by establishing a variational principle to analyze crack initiation and evolution. Subsequently, Bourdin et al. [31] proposed a regularization framework for the Francfort-Marigo variational principle, known as the phase field model for fracture mechanics. Within the phase field method framework, several investigations have been conducted to explore the fracture behavior of electromechanical materials. For brittle piezoelectric materials experiencing small deformations, Wu and Chen [32] proposed a PF-CZM model, yielding results consistent with experimental measurements. Regarding soft dielectric elastomer, Moreno-Mateos et al. [33] discussed numerically and experimentally how electromechanical actuation modulates fracture performance. These studies demonstrate the applicability of the G-criterion to electromechanical materials, whether under small or finite deformations.

This study presents a phase field fracture model tailored for flexible piezoelectrics subjected to finite deformations. The model incorporates various electrical boundary conditions at the crack surfaces. The subsequent sections are structured as follows: Sect. 2 outlines the derivation of governing equations and boundary conditions. Section 3 provides detailed information about the finite element implementation of the phase field model. An efficient staggered scheme, namely RCSA, is used to solve for the displacement, electric potential, and phase field variables. Several numerical examples are performed in Sect. 4 to demonstrate the effectiveness and applicability of the proposed model. Finally, we draw some conclusions in Sect. 5.

2 Governing equations

As shown in Fig. 1a, consider a cracked piezoelectric material, denoted as B_r, undergoing finite deformation. The boundary of the material is represented by ∂B_r, while the crack surface is denoted by Γ. An arbitrary material point $\mathbf{X}$ in the undeformed reference configuration B_r is mapped to $\mathbf{x}$ in the deformed configuration B_t. The deformation gradient is denoted as $\mathrm{F} = \partial \mathrm{x}/\partial \mathrm{X}$. To quantify the deformation, the Green–Lagrange strain is utilized, defined by $\mathbf{g} = \frac{1}{2}\left(\mathrm{F}^{\mathrm{T}}\mathrm{F} - \mathrm{I}\right)$, where$\mathbf{I}$ represents the identity tensor.

In the phase field method, crack propagation is formulated using a variable $\alpha(\mathbf{X},t)$, which indicates the degree of sharpness of the crack. The sharp crack is regularized by a diffuse crack $\Gamma_{l_0}(\alpha)$ in Fig. 1b. The variable α ranges from 0 to 1, where $\alpha = 0$ denotes an undamaged state of the material, and $\alpha = 1$ corresponds to a fully broken state. The total internal energy can be defined as

$$W_{int} = \int_{B_r} \psi_{em}\left(\mathrm{F}, \tilde{\mathrm{E}}\right) dV_0 + \int_{\Gamma} G_c d\Gamma + \int_{B_r} \frac{1}{2}\frac{\eta}{\Delta t}(\alpha - \alpha_n)^2 dV_0. \tag{1}$$

where, ψ_{em} represents the mixed energy-enthalpy per unit volume. G_c is the critical energy release rate. The third part denotes a viscous term [34], with η being the viscous parameter. α_n is the converged phase field variable at the previous increment with $\Delta t = t_{n+1} - t_n$.

The energy density ψ_{em} can be additively decomposed into [19]

$$\psi_{em} = g_m(\alpha)\psi_m(\mathrm{F}) + g_c(\alpha)\psi_c\left(\mathrm{F}, \tilde{\mathrm{E}}\right) + g_e(\alpha, \zeta)\psi_e\left(\tilde{\mathrm{E}}\right). \tag{2}$$

Herein, $g_m(\alpha)$, $g_c(\alpha)$, and $g_e(\alpha,\zeta)$ represent functions that describe the degradation of mechanical, coupled, and electric energy density, respectively. The ratio of electric permittivity between the crack ϵ_c and piezoelectric material ϵ_p is denoted by ζ, which can affect the fracture behavior of piezoelectric materials. This dimensionless variable ranges from 0 to 1, where a value of 1 indicates a perfectly electrically permeable crack, 0.5 indicates an electrically semi-permeable crack, and 0 indicates an electrically impermeable crack.

To simplify the computation of the fracture energy, an approximation can be used to avoid the need for cumbersome discontinuous surface integrals [35]. The second term of Eq. (1) can be recast as [35]

$$\int_{\Gamma} G_c d\Gamma \approx \int_{B_r} G_c \left(\frac{\alpha^2}{2l_0} + \frac{l_0}{2} \frac{\partial \alpha}{\partial X_i} \frac{\partial \alpha}{\partial X_i} \right) dV_0, \tag{3}$$

where the parameterl_0 controls the width of the smooth approximation of the crack.

In the absence of body forces and volumetric free charge density, the external energy of piezoelectric solid can be straightforwardly presented as

$$W_{ext} = \int_{S_{\mathrm{t}}} \mathrm{t} \cdot \mathrm{u} dA - \int_{S_w} w\phi dA. \tag{4}$$

where $\mathbf{u}$ is the displacement. ϕ represents the electric potential. $\mathbf{t}$ and w are the traction force per unit area applied on boundary $S_{\mathbf{t}}$ and surface free charge density applied on boundary S_w, respectively. The referential electric field intensity is defined as the gradient of electric potential, $\tilde{\mathrm{E}} = -\partial\phi(\mathrm{X}, t)/\partial \mathrm{X}$. Likewise, the spatial electric field intensity is represented as $\mathrm{E} = -\partial\phi(\mathrm{x}, t)/\partial \mathrm{x}$.

Based on the Neo-Hookean material model and electromechanical theory, our recent study proposed a novel nonlinear model [9] to investigate the finite deformation behavior of anisotropic flexible piezoelectric materials. Generally, an anisotropic crack surface density function is essential for accurately capturing the fracture behavior of anisotropic materials, as highlighted in previous studies [19, 36]. It has been reported that an isotropic model offers a simpler formulation for capturing mechanical behaviors [13] compared with the anisotropic model. In actuality, the fracture energy function described in Eq. (3) is more suitable for scenarios involving isotropic fracture toughness.

To simplify our analysis, we neglect the anisotropic properties of the flexible material in this study. The energy density has the form of [9]:

$$\begin{aligned}
\psi_m(\mathrm{F}) &= \frac{\mu}{2}\left(\overline{I}_1 - 3\right) + \frac{K_0}{2}(J-1)^2, \\
\psi_c\left(\mathrm{F}, \tilde{\mathrm{E}}\right) &= -J F^{-1}_{im} e_{mpq} \gamma_{pq} \tilde{E}_i, \\
\psi_e\left(\tilde{\mathrm{E}}\right) &= -\frac{1}{2} J F^{-1}_{im} \epsilon_{mj} F^{-1}_{kj} \tilde{E}_k \tilde{E}_i.
\end{aligned} \tag{5}$$

where, $\overline{I}_1 = J^{-2/3}\mathrm{tr}(\mathrm{F}^{\mathrm{T}}\mathrm{F})$. $J = \det(\mathbf{F})$. μ and K_0 represent the initial shear and bulk moduli, respectively. The symbols ϵ_{ij}, e_{ijk}, and γ_{jk} are used to denote dielectric, piezoelectric, and strain tensors, respectively. Herein, an isotropic flexible piezoelectric model is employed to investigate the fracture behavior. Future work will focus on enhancing the phase field model to account for variations in anisotropic fracture toughness, addressing a current limitation of the present study.

Substituting Eq. (5) into Eq. (2), the first Piola–Kirchhoff stress S_{ij} is derived as

$$\begin{aligned}
S_{ij} = \frac{\partial \psi_{em}}{\partial F_{ij}} &= g_m(\alpha)\left[\mu J^{-\frac{2}{3}}\left(F_{ij} - \frac{1}{3} I_1 F^{-1}_{ji}\right) + K_0 J(J-1)F^{-1}_{ji}\right] \\
&+ g_c(\alpha)\left[-J F^{-1}_{ji} F^{-1}_{lm} e_{mpq}\gamma_{pq}\tilde{E}_l + J F^{-1}_{jm} F^{-1}_{li} e_{mpq}\gamma_{pq}\tilde{E}_l - J F^{-1}_{lm} e_{mjq} F_{iq} \tilde{E}_l\right] \\
&+ g_e(\alpha, \zeta)\left[-\frac{1}{2} J F^{-1}_{ji} F^{-1}_{lm} \epsilon_{mn} F^{-1}_{kn} \tilde{E}_k \tilde{E}_l + J F^{-1}_{lm} \epsilon_{mn} F^{-1}_{jn} F^{-1}_{ki} \tilde{E}_k \tilde{E}_l\right].
\end{aligned} \tag{6}$$

The Cauchy stress σ_{ij} takes the form of

$$\begin{aligned}\sigma_{ij} = J^{-1}S_{ik}F_{jk} = g_m(\alpha)\left[\mu J^{-\frac{5}{3}}\left(F_{ik}F_{jk} - \frac{1}{3}I_1\delta_{ij}\right) + K_0(J-1)\delta_{ij}\right] \\ + g_c(\alpha)\left[-\delta_{ij}e_{mkl}\gamma_{kl}E_m + e_{jkl}\gamma_{kl}E_i - e_{mkl}F_{il}F_{jk}E_m\right] \\ + g_e(\alpha,\zeta)\left[-\delta_{ij}\frac{1}{2}\epsilon_{mn}E_nE_m + \epsilon_{nj}E_iE_n\right].\end{aligned} \tag{7}$$

The referential electric displacement $\tilde{D}_i$ and spatial electric displacement D_i can be expressed as

$$\tilde{D}_i = -\frac{\partial\psi_{em}}{\partial\tilde{E}_i} = g_c(\alpha)JF^{-1}_{im}e_{mpq}\gamma_{pq} + g_e(\alpha,\zeta)JF^{-1}_{im}\epsilon_{mj}F^{-1}_{kj}\tilde{E}_k, \tag{8}$$

$$D_i = J^{-1}F_{ij}\tilde{D}_j = g_c(\alpha)e_{ijk}\gamma_{jk} + g_e(\alpha,\zeta)\epsilon_{ij}E_j, \tag{9}$$

respectively.

Recall Eqs. (1), (2), (3), and (5), the variational of the total internal energy can be formulated as

$$\delta W_{int} = \frac{\partial W_{int}}{\partial \mathrm{F}} : \nabla\delta\mathrm{u} + \frac{\partial W_{int}}{\partial\tilde{\mathrm{E}}}\cdot\delta\tilde{\mathrm{E}} + \frac{\partial W_{int}}{\partial\alpha}\delta\alpha + \frac{\partial W_{int}}{\nabla\partial\alpha}\cdot\nabla\delta\alpha. \tag{10}$$

where

$$\begin{aligned}\frac{\partial W_{int}}{\partial \mathrm{F}} = \int_{B_r}\frac{\partial\psi_{em}}{\partial \mathrm{F}}dV_0 = \int_{B_r}\mathrm{S}dV_0, \frac{\partial W_{int}}{\partial\tilde{\mathrm{E}}} = \int_{B_r}\frac{\partial\psi_{em}}{\partial\tilde{\mathrm{E}}}dV_0 = -\int_{B_r}\tilde{\mathrm{D}}dV_0, \\ \frac{\partial W_{int}}{\partial\alpha} = \int_{B_r}\left(\frac{\partial\psi_{em}}{\partial\alpha} + \frac{\alpha}{l_0}G_c + \frac{\eta}{\Delta t}(\alpha-\alpha_n)\right)dV_0, \frac{\partial W_{int}}{\nabla\partial\alpha} = \int_{B_r}l_0G_c\nabla\alpha dV_0,\end{aligned} \tag{11}$$

with

$$\frac{\partial\psi_{em}}{\partial\alpha} = \frac{\partial g_m(\alpha)}{\partial\alpha}\psi_m(\mathrm{F}) + \frac{\partial g_c(\alpha)}{\partial\alpha}\psi_c\left(\mathrm{F},\tilde{\mathrm{E}}\right) + \frac{\partial g_e(\alpha,\zeta)}{\partial\alpha}\psi_e\left(\tilde{\mathrm{E}}\right). \tag{12}$$

With the help of Eq. (4), the formulation for the variational of external work can be expressed as

$$\delta W_{ext} = \int_{S_\mathrm{t}}\mathrm{t}\cdot\delta\mathrm{u}dA - \int_{S_w}w\delta\phi dA. \tag{13}$$

Using the principle of virtual work $\delta W_{int} - \delta W_{ext} = 0$, the strong forms of governing equations can be obtained by

$$\begin{aligned}&\frac{\partial \mathrm{S}}{\partial \mathrm{X}} = 0, \quad \text{in } B_r, \\ &\frac{\partial\tilde{\mathrm{D}}}{\partial \mathrm{X}} = 0, \quad \text{in } B_r, \\ &G_c\left(l_0\frac{\partial^2\alpha}{\partial \mathrm{X}^2} - \frac{\alpha}{l_0}\right) - \frac{\partial\psi_{em}}{\partial\alpha} - \frac{\eta}{\Delta t}(\alpha-\alpha_n) = 0, \quad \text{in } B_r,\end{aligned} \tag{14}$$

with the following boundary conditions

$$\begin{aligned}&\mathrm{S}\cdot\mathrm{n} = \mathrm{t}, \quad \text{on } S_\mathrm{t}, \\ &\tilde{\mathrm{D}}\cdot\mathrm{n} = -w, \quad \text{on } S_w, \\ &\frac{\partial\alpha}{\partial \mathrm{X}}\cdot\mathrm{n} = 0 \quad \text{on } \partial B_r,\end{aligned} \tag{15}$$

where $\mathbf{n}$ denotes the outward unit normal on the boundary ∂B_r.

In order to deal with fracture problems of brittle piezoelectric ceramics under different electrical boundary conditions along cracks, Sridhar and Keip [19] proposed various forms for electromechanical energy degradation functions. In this work, we employ the degradation functions of [13, 19]

$$g_m(\alpha) = g_c(\alpha) = (1-\alpha)^2 + k,$$

$$g_e(\alpha,\zeta) = 1 - 2(1-\zeta)\alpha + (1-\zeta)\alpha^2 + k, \tag{16}$$

where k is a small positive parameter to avoid numerical singularities during calculations. Notably, the introduction of parameter k is necessary for nonlinearly elastic materials. For the electrically permeable case, namely $\zeta = 1$, the function has the form of $g_e(\alpha,\ 1) = 1 + k$. While for the impermeable case, one obtains $g_m(\alpha) = g_c(\alpha) = g_e(\alpha,\ 0)$.

Previous studies [32, 37] reported that crack propagation in piezoelectric materials is derived from mechanical energy density. The mechanical energy density has the form of [32]

$$\psi_v\left(\mathrm{F},\tilde{\mathrm{E}}\right) = \psi_m(\mathrm{F}) + \psi_c\left(\mathrm{F},\tilde{\mathrm{E}}\right). \tag{17}$$

Notably, to ensure that material damage is only driven by tensile load, the above expression could be further additively decomposed into an active part ψ_v^+ caused by tension and an inactive part ψ_v^- caused by compression, respectively defined as

$$\begin{aligned}
\psi_v^+\left(\mathrm{F},\tilde{\mathrm{E}}\right) &= \frac{\mu}{2}\left(\overline{I}_1 - 3\right) - J\mathbf{g}^+ : \mathrm{e}^{\mathrm{T}} \cdot \mathrm{E} + H(J-1)\left[\frac{K_0}{2}(J-1)^2\right], \\
\psi_v^-\left(\mathrm{F},\tilde{\mathrm{E}}\right) &= -J\mathbf{g}^- : \mathrm{e}^{\mathrm{T}} \cdot \mathrm{E} + [1 - H(J-1)]\left[\frac{K_0}{2}(J-1)^2\right].
\end{aligned} \tag{18}$$

where $H(\cdot)$ represents the Heaviside function. $\mathbf{g}^{\pm} = \sum \langle \gamma_a \rangle^{\pm} n_a \otimes n_a$, γ_a and n_a denote the eigenvalue and eigenvector of the strain, respectively.

The last part in Eq. (14) could be recast as

$$G_c\left(l_0 \frac{\partial^2 \alpha}{\partial \mathrm{X}^2} - \frac{\alpha}{l_0}\right) + 2(1-\alpha)\psi_v^+\left(\mathrm{F},\tilde{\mathrm{E}}\right) - \frac{\eta}{\Delta t}(\alpha - \alpha_n) = 0, \quad \text{in } B_r. \tag{19}$$

To avoid crack healing after unloading, some studies [27] introduced a history field as the maximum electromechanical fracture source, defined as

$$\mathcal{H}(\mathrm{X},t) = \max_{\tau \in [0,t]} \psi_v^+(\mathrm{X},\tau). \tag{20}$$

Substituting Eq. (20) into Eq. (19) leads to the phase field evolution description

$$G_c\left(l_0 \frac{\partial^2 \alpha}{\partial \mathbf{X}^2} - \frac{\alpha}{l_0}\right) + 2(1-\alpha)\mathcal{H} - \frac{\eta}{\Delta t}(\alpha - \alpha_n) = 0. \tag{21}$$

3 Finite element implementation

In the finite element implementation, it is more convenient to work with weak forms of governing equations that can be discretized and solved using numerical methods. By employing the Galerkin approach, the weak forms can be obtained by

$$\begin{aligned}
&\int_{B_r} \mathrm{S} : \nabla \delta \mathrm{u} dV_0 = \int_{S_\mathrm{t}} \mathrm{t} \cdot \delta \mathrm{u} dA, \\
&\int_{B_r} \tilde{\mathrm{D}} \cdot \nabla \delta\phi dV_0 = -\int_{S_w} w\delta\phi dA, \\
&\int_{B_r} G_c\left(\frac{1}{l_0}\alpha\delta\alpha + l_0 \nabla\alpha \cdot \nabla\delta\alpha\right) dV_0 + \int_{B_r} \frac{\eta}{\Delta t}(\alpha - \alpha_n)\delta\alpha dV_0 - \int_{B_r} 2(1-\alpha)\mathcal{H}\delta\alpha dV_0 = 0.
\end{aligned} \tag{22}$$

3.1 Discretization

To simulate the phase field fracture of flexible piezoelectric materials, a numerical framework is employed using a two-dimensional four-noded quadrilateral element. The implementation of this framework is carried out in the commercial software ABAQUS by utilizing a user element subroutine UEL. The nodal solution variables for each element include displacement component $\mathbf{u}$, electric potential ϕ, and phase field variable α. These variables can be discretized as follows:

$$u_i = \sum u_i^A N^A (i = 1, 2), \quad \phi = \sum \phi^A N^A, \quad \alpha = \sum \alpha^A N^A \tag{23}$$

Herein, the superscript $A = 1, 2, 3, 4$ denotes the number of nodes per element. N^A represents the shape function associated with node A. The displacement, electric potential, and phase field values at node A are represented by u_i^A, ϕ^A and α^A, respectively.

3.2 Residuals and stiffness matrices

In the user element subroutine, the residual vector and element stiffness matrix must be calculated. Specifically, by substituting the nodal solution variable discretizations into the weak forms presented in Eq. (22), the elements residuals for displacement, electric potential, and phase field evolution can be derived by

$$\begin{aligned}
R_{u_i}^A &= -\int_{B_r^e} S_{ij} \frac{\partial N^A}{\partial X_j} dV_0 + \int_{S_t^e} N^A t_i dA, \\
R_{\phi}^A &= \int_{B_r^e} \tilde{D}_i \frac{\partial N^A}{\partial X_i} dV_0 + \int_{S_w^e} N^A w dA, \\
R_{\alpha}^A &= \int_{B_r^e} \left[G_c \frac{\alpha}{l_0} - 2(1-\alpha)\mathcal{H} + \frac{\eta}{\Delta t}(\alpha - \alpha_n) \right] N^A dV_0 + \int_{B_r^e} G_c l_0 \nabla \alpha \frac{\partial N^A}{\partial X_i} dV_0,
\end{aligned} \tag{24}$$

respectively.

If there are no surface tractions or surface charge density, the corresponding tangents can be calculated by

$$\begin{aligned}
K_{u_i^A u_k^B} &= -\frac{\partial R_{u_i}^A}{\partial u_k^B} = \int_{B_r^e} \frac{\partial N^A}{\partial X_j} \frac{\partial S_{ij}}{\partial F_{kn}} \frac{\partial N^B}{\partial X_n} dV_0 = \int_{B_t^e} \frac{\partial N^A}{\partial x_a} \left(J^{-1} F_{aj} F_{mn} \frac{\partial S_{ij}}{\partial F_{kn}} \right) \frac{\partial N^B}{\partial x_m} dV, \\
K_{u_i^A \phi^B} &= -\frac{\partial R_{u_i}^A}{\partial \phi^B} = -\int_{B_r^e} \frac{\partial N^A}{\partial X_j} \frac{\partial S_{ij}}{\partial \tilde{E}_l} \frac{\partial N^B}{\partial X_l} dV_0 = -\int_{B_t^e} \frac{\partial N^A}{\partial x_a} \left(J^{-1} F_{aj} F_{ml} \frac{\partial S_{ij}}{\partial \tilde{E}_l} \right) \frac{\partial N^B}{\partial x_m} dV, \\
K_{\phi^A u_i^B} &= -\frac{\partial R_{\phi}^A}{\partial u_i^B} = -\int_{B_r^e} \frac{\partial N^A}{\partial X_l} \frac{\partial \tilde{D}_l}{\partial F_{in}} \frac{\partial N^B}{\partial X_n} dV_0 = -\int_{B_t^e} \frac{\partial N^A}{\partial x_a} \left(J^{-1} F_{al} F_{jn} \frac{\partial \tilde{D}_l}{\partial F_{in}} \right) \frac{\partial N^B}{\partial x_j} dV, \\
K_{\phi^A \phi^B} &= -\frac{\partial R_{\phi}^A}{\partial \phi^B} = \int_{B_r^e} \frac{\partial N^A}{\partial X_l} \frac{\partial \tilde{D}_l}{\partial \tilde{E}_i} \frac{\partial N^B}{\partial X_i} dV_0 = \int_{B_t^e} \frac{\partial N^A}{\partial x_a} \left(J^{-1} F_{al} F_{ji} \frac{\partial \tilde{D}_l}{\partial \tilde{E}_i} \right) \frac{\partial N^B}{\partial x_j} dV, \\
K_{\alpha^A \alpha^B} &= -\frac{\partial R_{\alpha}^A}{\partial \alpha^B} = \int_{B_r^e} -\left(2\mathcal{H} + \frac{G_c}{l_0} + \frac{\eta}{\Delta t} \right) N^A N^B dV_0 - \int_{B_r^e} G_c l_0 \frac{\partial N^A}{\partial X_i} \frac{\partial N^B}{\partial X_i} dV_0 \\
&= \int_{B_t^e} -J^{-1} \left(2\mathcal{H} + \frac{G_c}{l_0} + \frac{\eta}{\Delta t} \right) N^A N^B dV - \int_{B_t^e} \frac{\partial N^A}{\partial x_k} \left(J^{-1} F_{ki} F_{li} G_c l_0 \right) \frac{\partial N^B}{\partial x_l} dV.
\end{aligned} \tag{25}$$

Herein, B_t^e represents the discrete deformable body and satisfies $B_t = \cup B_t^e$. Particularly, the tangent stiffness matrices $\mathbf{K_{uu}}$, $\mathrm{K_{u\phi}}$, $\mathrm{K_{\phi u}}$ and $\mathrm{K_{\phi\phi}}$ have the same expression as described in the literature [9]. However, the first Piola–Kirchhoff stress and electric displacement in Eq. (25) incorporate the degradation functions.

Table 1 Materials properties of $BaTiO_3$ [13]

Property	Value
Young's modulus (GPa)	$E = 116.1331$
Passion ratio	$\nu = 0.31967$
Piezoelectric parameter (C/m^2)	$e_{311} = -4.4$ $e_{333} = 18.6$ $e_{113} = 11.6$
Dielectric (10^{-9} F/m)	$\epsilon_{11} = 11.2$ $\epsilon_{33} = 12.6$
Critical energy release rate (N/m)	$G_c = 200$
Length scale parameter (mm)	$l_0 = 0.01$

3.3 Staggered algorithm

Staggered algorithm is robust in solving nonlinear governing equations [38]. According to the different stop or coverage criteria, staggered algorithms can be classified into single-pass [29, 39], damage-based [40], energy-based [41], and residual-based [13, 36, 42] criteria. In consideration of the easy implementation and insensitivity to load increments of RCSA, this algorithm is employed to address the fracture failure problem of finite deformation for flexible piezoelectric solids. Details of the RCSA scheme can be found in the literature [42].

4 Numerical examples

During the simulations, if convergence is not achieved, the loading step size will be automatically reduced. Notably, to prevent complete loss of stiffness in a fully damaged element, a small parameter $k = 1 \times 10^{-5}$ is adopted throughout this work. This parameter helps maintain some residual stiffness even in elements that have undergone significant damage.

4.1 Single-edge notched tension test

To validate the numerical implementation, a square piezoelectric plate model is established in Fig. 2a. There is an initial sharp crack with a length of 0.5 mm in the middle of the specimen. The bottom edge is fixed, maintaining a zero electric potential. The top edge undergoes displacement loading, accompanied by the application of an electric potential of ϕ^*. To investigate the influence of poling direction on fracture behavior, cases of parallel and perpendicular to electric field direction are involved. The material parameters utilized in this work are consistent with the literature [13], as listed in Table 1. Notably, the current nonlinear electromechanical material model is isotropic, whereas Tan et al. [13] utilized a transversely isotropic piezoelectric model with smaller values of elastic constants c_{33} and c_{44}. To properly capture the behavior of crack propagation, a refined discretization strategy is employed in regions where the crack has the potential to propagate. This leads to a finite element mesh consisting of 26,045 elements. A displacement increment Δu of 4×10^{-5} mm is employed. Consistent with the literature [13], the viscous parameter η is set to zero in this example.

4.1.1 Poling directing parallel to electric field direction

In this case, the poling direction aligns parallel to the electric field direction. At an applied electric potential of $\phi^* = -1000$ V, Fig. 2b–e presents phase field contour, electric potential distributions, and electric field distributions for various electrical boundary conditions upon the complete fracture. These boundary conditions include impermeable $\zeta = 0$ in Fig. 2c, semi-permeable $\zeta = 0.5$ in Fig. 2d, and perfectly permeable $\zeta = 1$ cases in Fig. 2e. Under the tensile and electric loadings, the material exhibits fracture behavior with crack propagating from the initial notch toward the right side. Significant variations are observed in the electric potential and electric field distributions under different electrical boundary conditions. In the impermeable electrical boundary assumption, an electric potential discontinuity occurs in Fig. 2c(i). This is due to the impermeability of the crack to electric potential, causing a division in the internal electric potential. In contrast, both the semi-permeable and permeable cases maintain continuous electric potential along the predicted crack propagation path (Fig. 2d(i) and e(i)). This continuity is attributed to the permeability of the electric potential allowed by these conditions. Moreover, the electric field distributions within the crack also vary with the electrical

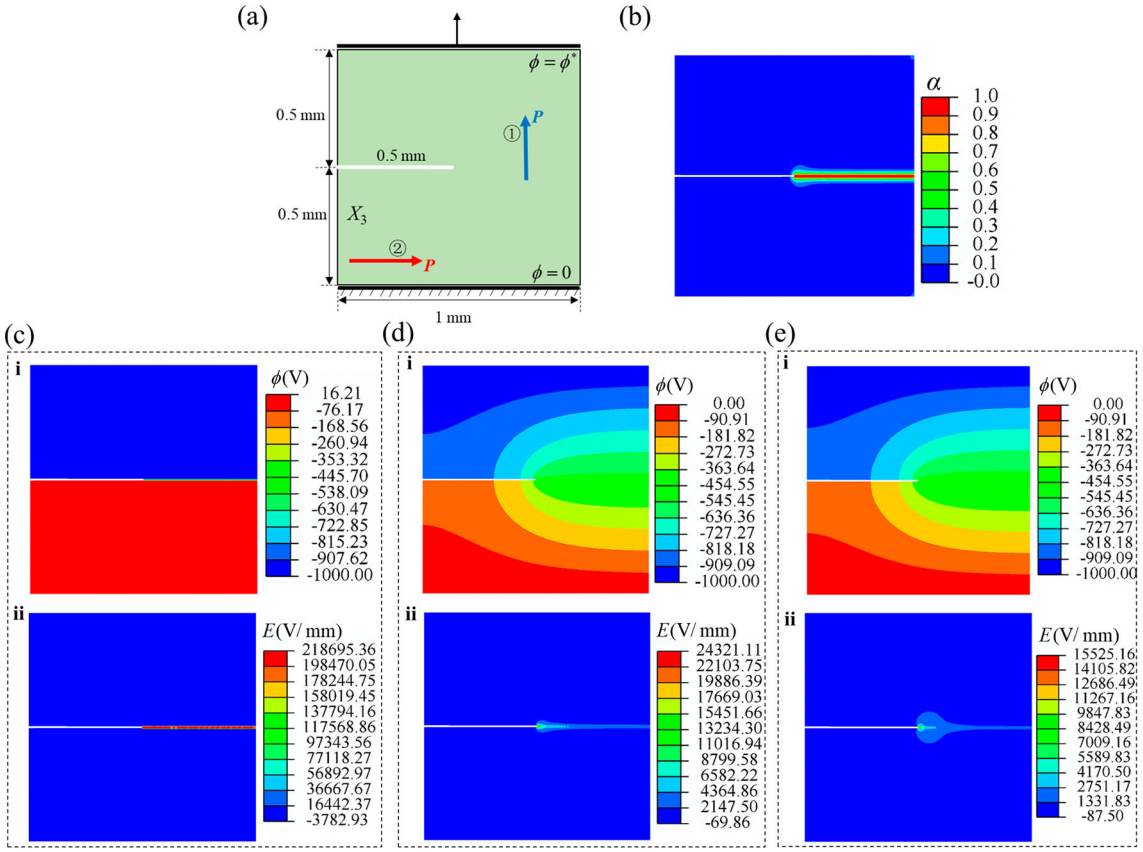

Fig. 2 Schematic diagram and response of a single-notched piezoelectric material. **a** Schematic illustration of the piezoelectric specimen subjected to uniaxial tension and an electric field. Upon the complete fracture with the applied electric potential ϕ^* of − 1000 V, **b** phase field contour, (i) electric potential distributions, and (ii) electric field distributions inside the material for the **c** impermeable, **d** semi-permeable, and **e** permeable electrical boundary conditions, respectively

boundary conditions. In the impermeable crack assumption (Fig. 2c(ii)), there is a high concentration of the electric field within the crack, sharply decreasing elsewhere. This occurs due to the abrupt change in electric potential across the crack surface. Under the semi-permeable condition (Fig. 2d(ii)), the electric field within the crack remains concentrated but with reduced magnitude. In contrast, in the permeable case (Fig. 2e(ii)), the electric field distribution within the crack is more uniform, indicating free propagation without significant hindrance or concentration. These observations highlight the influence of electrical boundary conditions on the crack behavior, electric potential, and electric field distributions.

Figure 3 illustrates the relationship between load and displacement under various applied electric potentials ranging from − 1000 V to 1000 V. When the poling direction is parallel to the electric field direction, the results under the assumption of electric impermeability are depicted in Fig. 3a. With the increasing in electric potential, both the ultimate displacement and peak load correspondingly increases, indicating delayed fracture occurrence. However, differences emerge in the semi-permeable case (Fig. 3b) and permeable case (Fig. 3c). In both scenarios, higher electric potential increases peak load while decreasing ultimate displacement. This discrepancy in ultimate displacement demonstrates the influence of electrical boundary conditions on fracture behavior. In Fig. 3d, the simulation results under different electrical boundary conditions with an applied electric potential ϕ^* of 1000 V are compared with the literature [13]. Peak loads of 156.42 N, 153.49 N, and 153.19 N are observed for impermeable, semi-permeable, and permeable scenarios, respectively. Interestingly, allowing electrical permeability results in a reduced fracture load for the brittle $BaTiO_3$ specimen, compared with the impermeable condition. In addition, it promotes the earlier occurrence of fracture. Furthermore, the predicted results fit well with the results reported in the literature. This simulation demonstrates the reliability and effectiveness of the numerical framework. Notably, material parameters utilized in this example result in the piezoelectric material fracturing at a small strain state. Consequently, the results obtained from the nonlinear

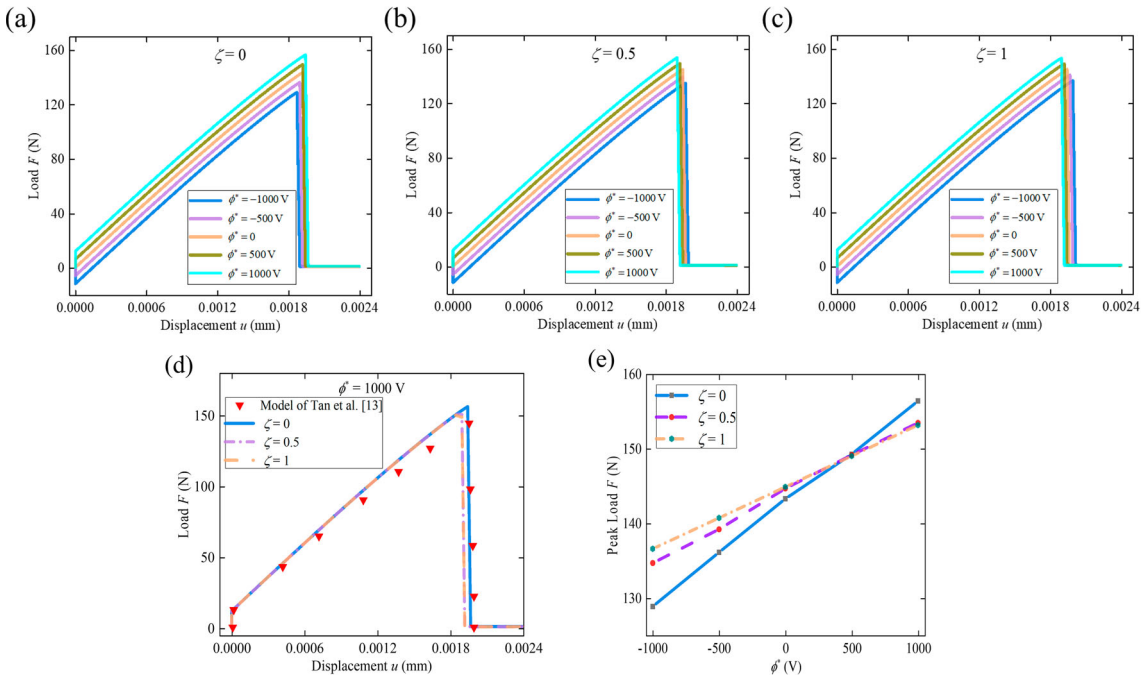

Fig. 3 When the poling direction is parallel to electric field direction, the relationship between load and displacement under various electric potentials ranging from − 1000 V to 1000 V. Load and displacement curves for the **a** impermeable, **b** semi-permeable, and **c** permeable cases, respectively. **d** At an applied electric potential of 1000 V, a comparison of results between obtained numerical simulations and literature data [13]. Dots and lines represent results from the literature [13] and numerical simulations, respectively. **e** The relation of peak load versus electric potential under different electrical boundary conditions

electromechanical material model do not exhibit significant differences from those using linear theory in the literature [13].

In Fig. 3e, the peak load exhibits a linear increase with higher electric potential. Under negative electric potential, the permeable case exhibits the highest peak load, followed by the semi-permeable case, and then the impermeable case. Notably, at an applied electric potential ϕ^* of 500 V, different electrical boundary conditions predict similar peak loads. However, at 1000 V, the impermeable case shows the highest peak load, while the permeable case demonstrates the smallest value.

4.1.2 Poling directing perpendicular to electric field direction

Figure 4a–d explore scenarios where the poling direction is perpendicular to the electric field direction. It can be observed that variations in electric potential do not significantly affect the load-bearing capability. Across different electrical boundary conditions, zero electric potential consistently results in the maximum peak load. Regarding ultimate displacement, similar trends are observed in both the impermeable case (Fig. 4a) and the semi-permeable case (Fig. 4b). Larger electric field magnitudes correspond to smaller ultimate displacements. In contrast, Fig. 4c indicates that the electric potential may not influence the ultimate displacement in the permeable case.

The relations of peak load versus electric potential are shown in Fig. 4d. Initially, peak load increases with higher electric potential, reaching a maximum at zero electric potential, and subsequently decreases. Furthermore, across different electric potentials, the impermeable case consistently shows the highest peak load, followed by the semi-permeable case, and then the permeable case.

These results indicate that the fracture behavior of the piezoelectric material is influenced by the electrical permeability of the crack. However, the specific effects can be different depending on the applied electric potential, and poling direction.

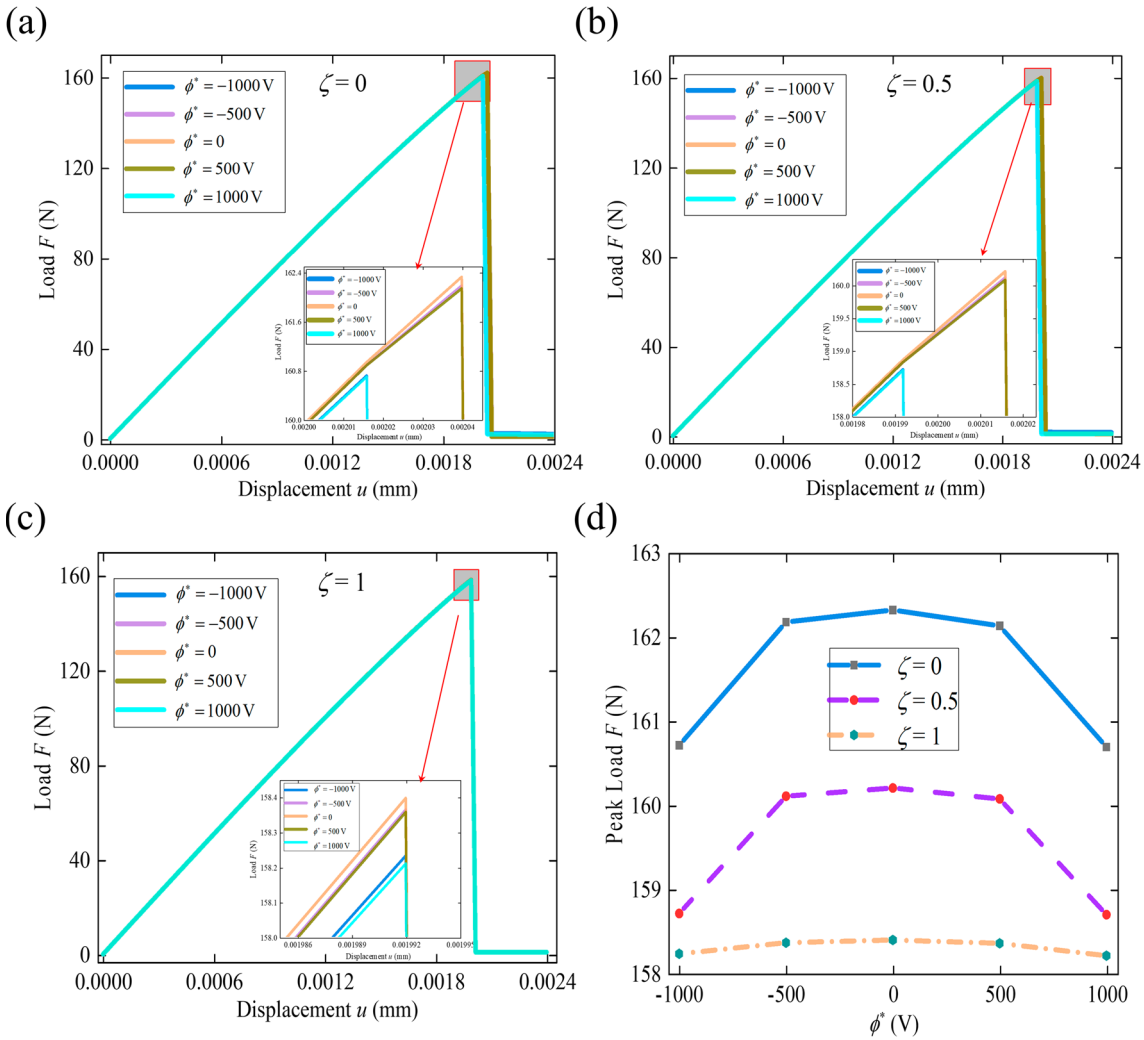

Fig. 4 When the poling direction is perpendicular to electric field direction, load and displacement relationships under various electric potentials ranging from − 1000 V to 1000 V. Load and displacement curves for the **a** impermeable, **b** semi-permeable, and **c** permeable cases, respectively. **d** Relationship between peak load and electric potential under different electrical boundary conditions

4.2 Three-point bending test

A three-point bending case of flexible piezoelectric material (PVDF) is considered in Fig. 5a. This specimen has a length of $L = 20$ mm, a width of $w = 10$ mm, and a height of $h = 5$ mm. There is a vertical slit inserted at the lower boundary to create a pre-crack with a length of 2 mm. Two different eccentricities of the crack are considered: one positioned at the mid-span (0 mm offset) and another with a 4 mm offset. The left support is constrained in both horizontal and vertical directions, while the right one is constrained vertically. A displacement loading is applied at the center of the upper edge, with an increment Δu of 2×10^{-2} mm. The left side maintains a zero electric potential, whereas an electric potential of ϕ^* is applied on the right side. The poling direction is denoted by $\boldsymbol{P}$. The material parameters used are listed in Table 2. In the region around the potential crack propagation path, the mesh is refined via the characterized element size of $l_0/3$. Different electrical boundary conditions of impermeable, semi-permeable, and permeable cases are considered. To avoid potential numerical convergence issues, a value of $\eta = 10^{-3}$ is adopted for all subsequent simulations.

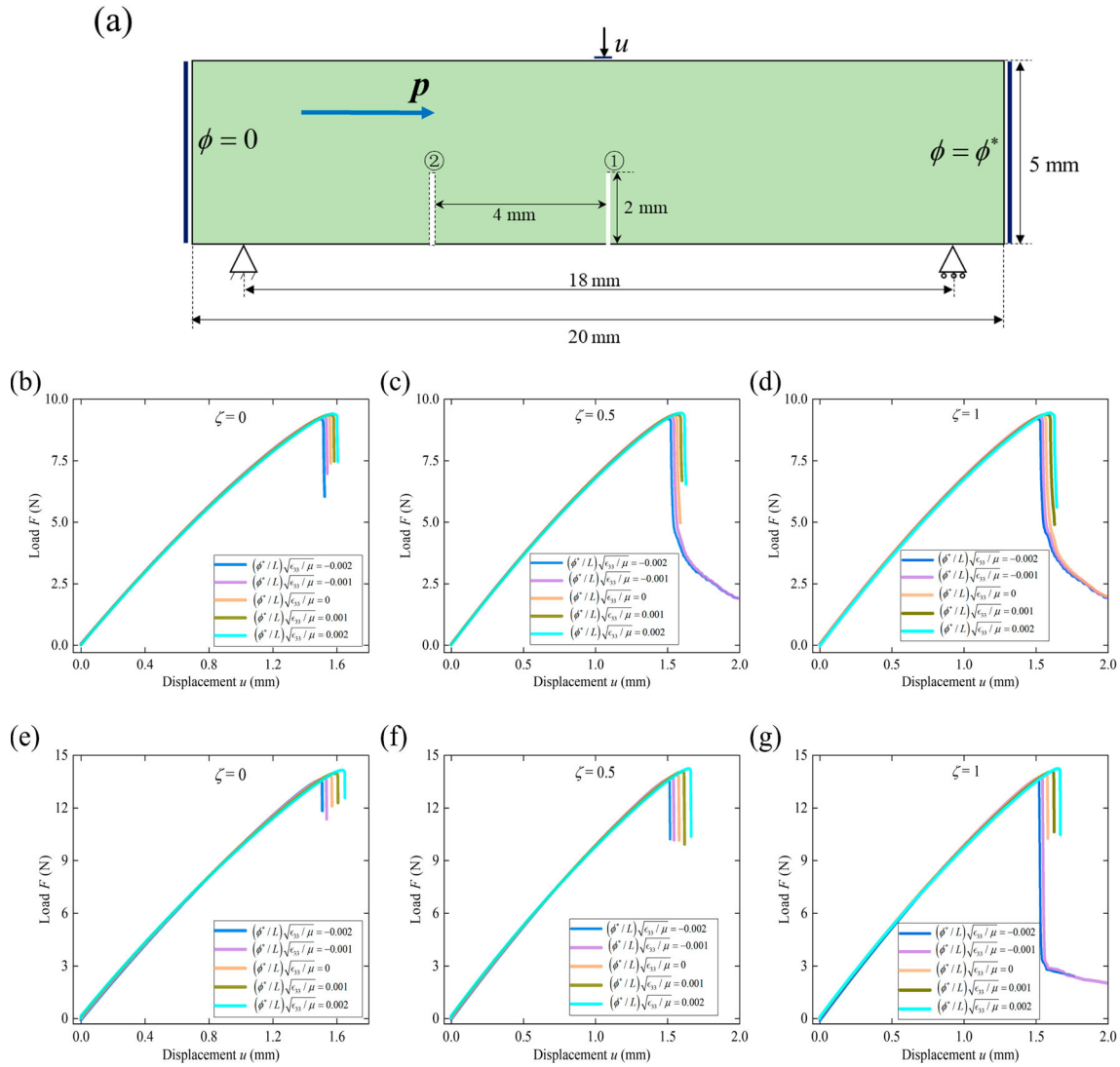

Fig. 5 When the poling direction is parallel to electric field direction, schematic representation and response of a flexible piezoelectric specimen in a three-point bending test. **a** Schematic diagram of the three-point bending test of a flexible piezoelectric specimen with a pre-crack, where the pre-crack has two different eccentricities: 0 mm, and 4 mm offset from the mid-span. At various normalized electric potentials $(\phi^*/L)\sqrt{\epsilon_{33}/\mu}$ ranging from $-$ 0.002 to 0.002: with a notch eccentricity of 0 mm, load–displacement curves for the **b** impermeable, **c** semi-permeable, and **d** permeable cases, respectively. With a notch eccentricity of 4 mm, load and displacement relationships for the **e** impermeable, **f** semi-permeable, and **g** permeable cases, respectively

Table 2 Materials properties of PVDF [9]

Property	Value
Young's modulus (MPa)	$E = 10$
Passion ratio	$\nu = 0.4$
Piezoelectric parameter (C/m^2)	$e_{311} = 0.11$ $e_{333} = -0.165$ $e_{113} = 0.07$
Dielectric (10^{-11} F/m)	$\epsilon_{11} = 4.87$ $\epsilon_{33} = 5.11$
Critical energy release rate (N/mm)	$G_c = 0.31$
Length scale parameter (mm)	$l_0 = 0.15$

4.2.1 Poling directing parallel to electric field direction

When the poling direction is parallel to the electric field direction, the schematic illustration is presented in Fig. 5a and the responses are shown in Fig. 5b–g.

A notch eccentricity of 0 mm In the case where the notch eccentricity is 0 mm, the predicted load–displacement curves are depicted in Fig. 5b–d. Initially, the force increases with the increase in loading displacement. When it reaches the maximum load, the crack begins to propagate towards the top side. With the further loading, the force gradually decreases. Similar trends are observed across different electrical boundary conditions: in Fig. 5b for the impermeable case, Fig. 5c for the semi-permeable case, and Fig. 5d for the permeable case. Specifically, peak load increases with higher electric potential, and ultimate displacement also rises under varying electrical conditions. This suggests that higher electric potential delays the fracture occurrence. Flexible piezoelectric materials exhibit a rapid decrease in load-bearing capacity after reaching their maximum load. However, with further loading and larger displacements, these materials can still maintain a certain level of load-bearing capacity.

A notch eccentricity of 4 mm In the case of a notch eccentricity of 4 mm, similar phenomena are observed compared to the previous case. Higher electric potential enhances the load-bearing capacity irrespective of the electrical boundary conditions: impermeable case in Fig. 5e, semi-permeable case in Fig. 5f, and permeable case in Fig. 5g. However, the peak load exhibits a higher value compared to the case with notch eccentricity of 0 mm.

To enhance the understanding of the effects of various electrical boundary conditions, Fig. 6 illustrates the distribution of stress and electric field in a flexible piezoelectric specimen as the initial crack begins to propagate. Under displacement loading, the top of the specimen experiences compressive stress, while the bottom experiences tensile stress. Regardless of the electrical boundary conditions (the impermeable case in Fig. 6a, the semi-permeable case in Fig. 6c, and the permeable case in Fig. 6e), a stress concentration phenomenon occurs at the crack tip. Similarly, the electric field distribution exhibits a peak at the crack tip, with the impermeable case exhibiting the highest electric field intensity (Fig. 6b), followed by the semi-permeable case (Fig. 6d) and the permeable case (Fig. 6f). This variation in electric field intensity highlights the influence of boundary conditions on the material's response to crack propagation.

Figure 7 demonstrates the relationship between peak load and applied electric potential. As electric potential increases, peak load also increases in both cases. Notably, the impermeable scenario consistently exhibits the lowest peak load in both cases. This indicates an enhanced bearing capacity when electrical permeability is allowed. In Fig. 7a, depicting the notch eccentricity of 0 mm, the relationship follows an approximate logarithmical model of increase. However, with a notch eccentricity of 4 mm in Fig. 7b, the relation follows an approximate exponential model.

4.2.2 Poling directing perpendicular to electric field direction

In addition, to investigate the influence of the poling direction, perpendicular orientation to the electric field direction is considered in Fig. 8a.

A notch eccentricity of 0 mm In the scenario with a notch eccentricity of 0 mm, the predicted load–displacement curves for impermeable, semi-permeable, and permeable cases are depicted in Fig. 8b, c, and d, respectively. The results indicate that the bearing capacity increases with increasing electric potential, although this trend shows a limited increment. After reaching the peak load, there is a gradual decline in bearing capacity. This suggests that the structure maintains a certain level of bearing capacity even under significant large displacement. This may be attributed to the high tensile limit of flexible materials, which can delay material failure. In contrast, brittle piezoelectric materials behave differently after reaching their maximum strength limit. Some studies [13, 32] have reported that once the maximum strength limit is reached, cracks rapidly propagate, leading to the loss of load-bearing capacity. In contrast to the case where the poling direction is parallel to the electric field direction, the ultimate load capacity of the structure diminishes.

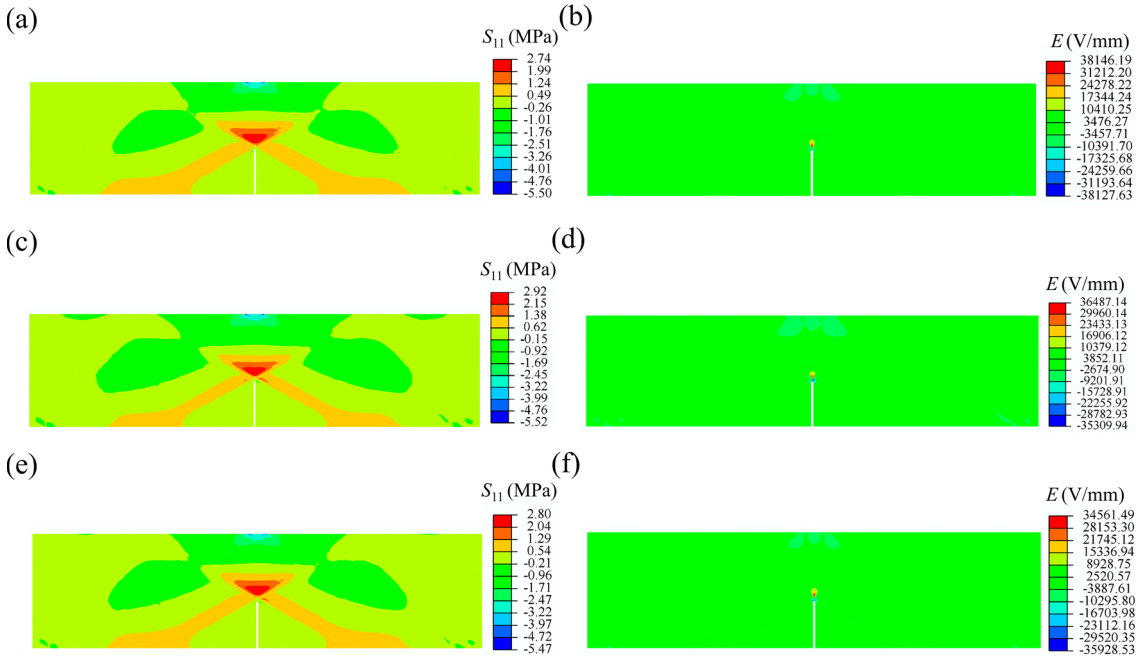

Fig. 6 Under the displacement loading, stress and electric field distributions under different electrical boundary conditions. In the impermeable case, the distribution of **a** stress and**b** electric field. **c** Stress distribution for the semi-permeable case, with the corresponding **d** electric field distribution. In the permeable case, the distribution of **e** stress and **f** electric field

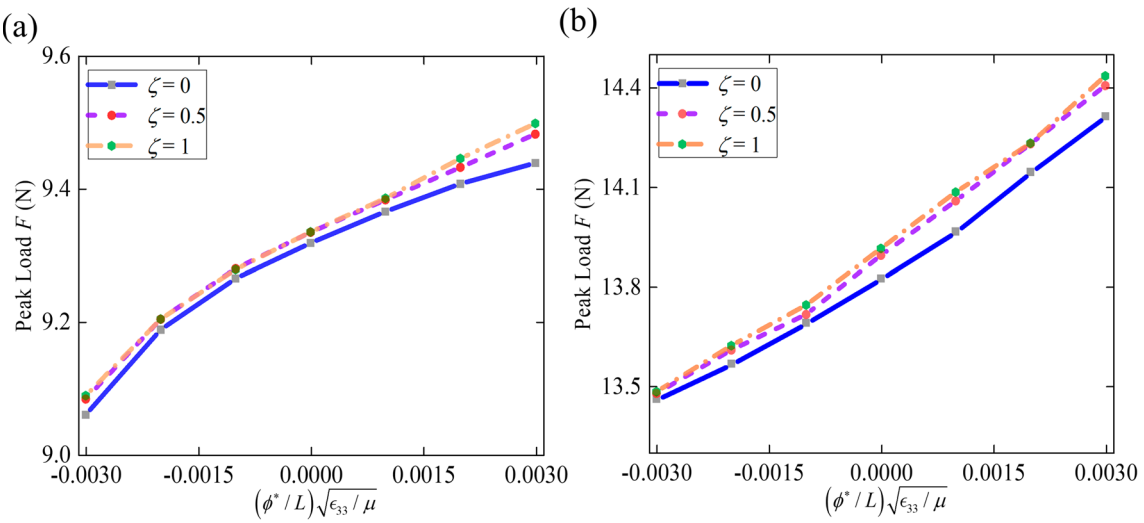

Fig. 7 In consideration of the poling direction parallel to electric field direction, peak load versus normalized electric potential $(\phi^*/L)\sqrt{\epsilon_{33}/\mu}$ with notch eccentricities of **a** 0 mm and **b** 4 mm offset from the mid-span, respectively

A notch eccentricity of 4 mm When the notch eccentricity is 4 mm, the simulation results for impermeable, semi-permeable, and permeable cases are presented in Fig. 8e–g, respectively. Interestingly, the peak load decreases with the increasing electric potential, while the ultimate displacement increases.

Figure 9 further illustrates the relation of peak load versus applied electric potential. In both notch eccentricity cases, the impermeable scenario consistently shows the lowest peak load. For a notch eccentricity of 0 mm in Fig. 9a, the peak load increases with increasing electric potential. Furthermore, the permeable case exhibits the maximum bearing capacity, followed by the semi-permeable case, and then the impermeable case. Conversely, in Fig. 9b, where the notch eccentricity is 4 mm, the peak load decreases with increasing electric potential. In this case, the electrically impermeable assumption results in the lowest peak load, while the semi-permeable case may yield the highest bearing capacity.

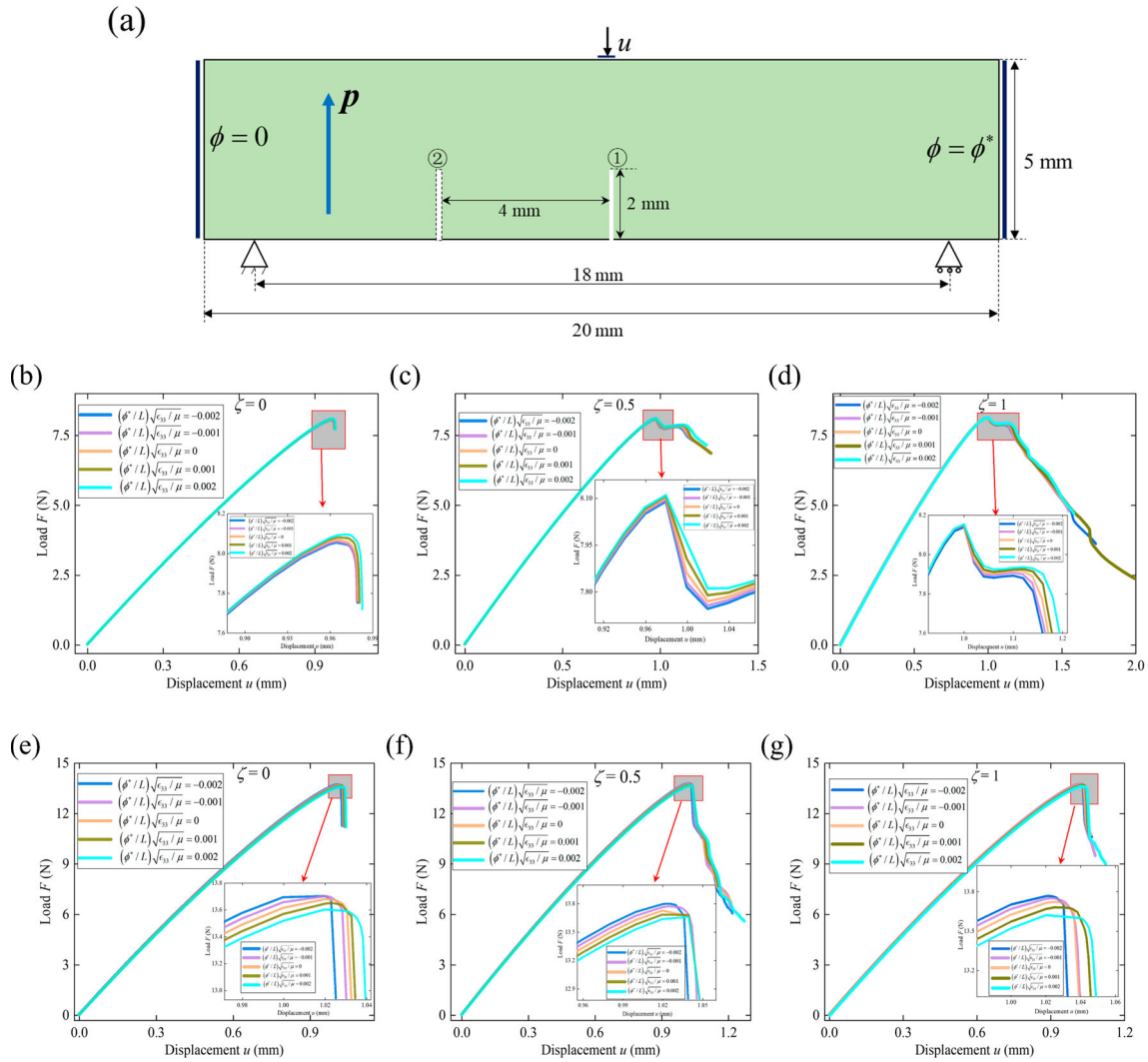

Fig. 8 When the poling direction is perpendicular to electric field direction, schematic representation and response of a flexible piezoelectric specimen in a three-point bending test. **a** Schematic diagram of the three-point bending test of a flexible piezoelectric specimen with a pre-crack. At various normalized electric potentials $(\phi^*/L)\sqrt{\epsilon_{33}/\mu}$ ranging from $-$ 0.002 to 0.002: with a notch eccentricity of 0 mm offset from the mid-span, load–displacement curves for the **b** impermeable, **c** semi-permeable, and **d** permeable cases, respectively. With a notch eccentricity of 4 mm, load and displacement relationships for the **e** impermeable, **f** semi-permeable, and **g** permeable cases, respectively

To demonstrate the influence of electromechanical response, comparisons of load–displacement curves are presented in Fig. 10, where zero electric potential is applied. Setting the piezoelectric and dielectric parameters to zero indicates the absence of electromechanical response. The results for notch eccentricities of 0 mm and 4 mm are shown in Fig. 10a and b, respectively. In both cases, the scenario with the poling direction aligned parallel to the electric field direction exhibits the highest peak load, followed by the perpendicular configuration. In contrast, the curve representing the absence of electromechanical response exhibits the lowest peak load. Notably, the ultimate displacement without electromechanical response is notably high.

5 Conclusion

In this contribution, a phase field model is proposed to predict the fracture behavior of flexible piezoelectrics under finite deformation and external electric fields. This model takes into account different electrical boundary conditions on the crack surfaces. The numerical simulations are implemented using the commercial finite

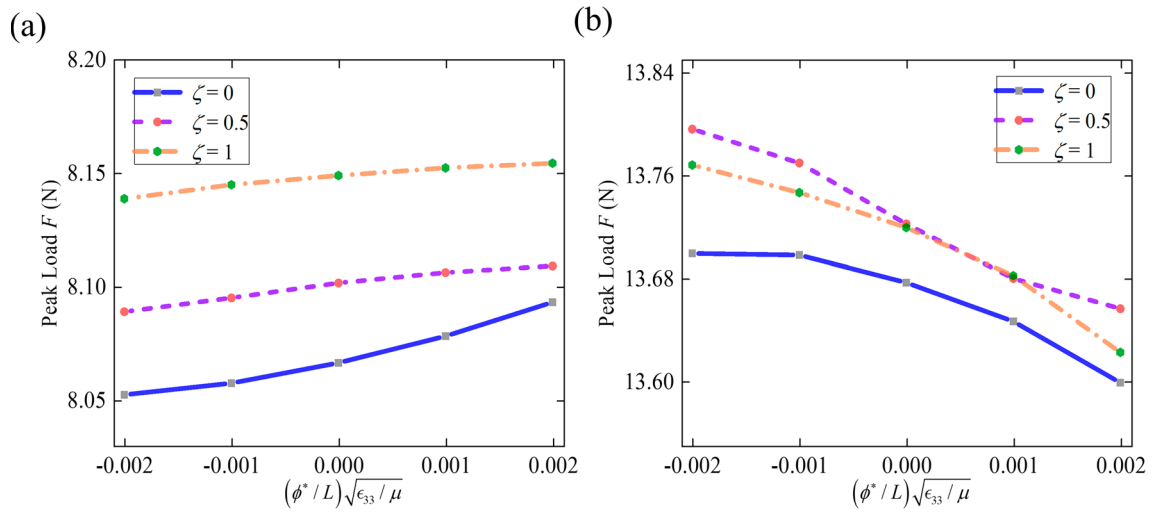

Fig. 9 Relationship between peak load and normalized electric potential $(\phi^*/L)\sqrt{\epsilon_{33}/\mu}$ under different electrical boundary conditions when the poling direction is perpendicular to the electric field direction. Peak load versus normalized electric potential with notch eccentricities of **a** 0 mm and **b** 4 mm offset from the mid-span, respectively

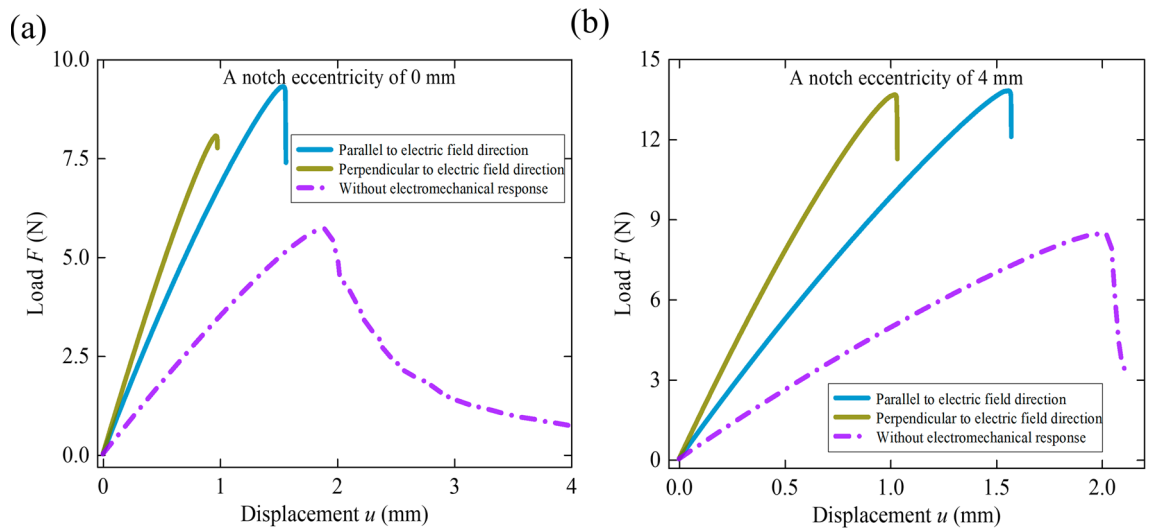

Fig. 10 Comparison of with and without electromechanical responses, for notch eccentricities of **a** 0 mm and **b** 4 mm offset from the mid-span, respectively. Results considering electromechanical response are obtained under the assumption of electrically impermeable and zero applied electric potential. Solid lines represent results with electromechanical response, while dashed lines correspond to results without electromechanical response

element software ABAQUS, utilizing a user element subroutine. RCSA scheme is employed to solve the coupled displacement, electric potential, and phase field variables.

Numerical simulations are conducted on single-edge notched tension and three-point bending tests. To investigate the influence of the poling direction on fracture behavior, both parallel and perpendicular orientations to electric field direction are considered. Results show that the fracture of piezoelectric materials is affected by poling direction, external electric fields, and electrical boundary conditions. In the case of single-edge notched tension, when the poling direction is parallel to the electric field direction, the electrical permeability influences the fracture load, with the specific effect depending on the magnitude of the applied electric field. Conversely, when the poling direction is perpendicular to the electric field direction, the presence of electrical permeability may reduce the fracture load. Regarding the three-point bending test, the presence of electrical permeability may increase the fracture load, regardless of the poling direction, in contrast to the conditions of electrical impermeability. When the poling direction is aligned with the electric field direction, an increase in electric potential results in a higher peak load. Conversely, when the poling direction is perpen-

dicular to the electric field direction, varying notch eccentricities result in differing effects of electric potential on bearing capacity.

The fracture behavior of flexible piezoelectric materials is influenced by geometric parameters, external electric fields, and the poling direction. This study aims to contribute to the development of guidelines for accurately predicting fractures in these materials under electromechanical environments.

Funding The authors would like to thank the supports from National Natural Science Foundation of China (NSFC) (12072150). This work is also supported by Beijing Nova Program (20230484287), National Natural Science Foundation of China for Creative Research Groups (No. 51921003).

Declarations

Conflict of interest The authors declare no conflict of interest.

References

1. Lv, S., Li, B., Zhang, Q., Shi, Y., Gao, C.: A finite deformation phase field model for electromechanical fracture of flexible piezoelectric materials. Appl. Math. Model. **130**, 728–748 (2024). https://doi.org/10.1016/j.apm.2024.03.032
2. Fan, F.R., Tang, W., Wang, Z.L.: Flexible nanogenerators for energy harvesting and self-powered electronics. Adv. Mater. **28**, 4283–4305 (2016). https://doi.org/10.1002/adma.201504299
3. Zhao, Z., Dai, Y., Dou, S.X., Liang, J.: Flexible nanogenerators for wearable electronic applications based on piezoelectric materials. Mater. Today Energy **20**, 100690 (2021). https://doi.org/10.1016/j.mtener.2021.100690
4. Ma, L., Melkote, S.N., Morehouse, J.B., Castle, J.B., Fonda, J.W., Johnson, M.A.: Design of thin-film polyvinylidene fluoride sensor rosettes for isolation of various strain components. J. Intell. Mater. Syst. Struct. **23**, 1119–1130 (2012). https://doi.org/10.1177/1045389X12443597
5. Kim, K., Kim, J., Jiang, X., Kim, T.: Static force measurement using piezoelectric sensors. J Sensors (2021). https://doi.org/10.1155/2021/6664200
6. Yoon, K., Kelarakis, A.: Nanoclay-directed structure and morphology in PVDF electrospun membranes. J. Nanomater. (2014). https://doi.org/10.1155/2014/367671
7. Shehata, N., Nair, R., Boualayan, R., Kandas, I., Masrani, A., Elnabawy, E., Omran, N., Gamal, M., Hassanin, A.H.: Stretchable nanofibers of polyvinylidenefluoride (PVDF)/thermoplastic polyurethane (TPU) nanocomposite to support piezoelectric response via mechanical elasticity. Sci. Rep. **12**, 8335 (2022). https://doi.org/10.1038/s41598-022-11465-5
8. Gao, C.F., Noda, N.: Faber series method for two-dimensional problems of an arbitrarily shaped inclusion in piezoelectric materials. Acta Mech. **171**, 1–13 (2004). https://doi.org/10.1007/s00707-004-0131-0
9. Lv, S., Meng, L., Zhang, Q., Shi, Y., Gao, C.: Numerical framework for anisotropic flexible piezoelectrics with large deformation. Int. J. Mech. Sci. **258**, 108564 (2023). https://doi.org/10.1016/j.ijmecsci.2023.108564
10. Landis, C.M.: Energetically consistent boundary conditions for electromechanical fracture. Int. J. Solids Struct. **41**, 6291–6315 (2004). https://doi.org/10.1016/j.ijsolstr.2004.05.062
11. Miehe, C., Welschinger, F., Hofacker, M.: A phase field model of electromechanical fracture. J. Mech. Phys. Solids **58**, 1716–1740 (2010). https://doi.org/10.1016/j.jmps.2010.06.013
12. Zhang, B., Luo, J.: A phase field model for electromechanical fracture in flexoelectric solids. Eng. Fract. Mech. **271**, 108564 (2022). https://doi.org/10.1016/j.engfracmech.2022.108564
13. Tan, Y., He, Y., Liu, C., Li, X.: Phase field fracture model of transversely isotropic piezoelectric materials with thermal effect. Eng. Fract. Mech. **268**, 108479 (2022). https://doi.org/10.1016/j.engfracmech.2022.108479
14. Wilson, Z.A., Borden, M.J., Landis, C.M.: A phase-field model for fracture in piezoelectric ceramics. Int. J. Fract. **183**, 135–153 (2013). https://doi.org/10.1007/s10704-013-9881-9
15. Parton, V.Z.: Fracture mechanics of piezoelectric materials. Acta Astronaut. **3**, 671–683 (1976). https://doi.org/10.1016/0094-5765(76)90105-3
16. Pak, Y.E.: Linear electro-elastic fracture mechanics of piezoelectric materials. Int. J. Fract. **54**, 79–100 (1992). https://doi.org/10.1007/BF00040857
17. Tian-Hu, H., Zi-Yuan, S.: A new electric boundary condition of electric fracture mechanics and its applications. Eng. Fract. Mech. **47**, 793–802 (1994). https://doi.org/10.1016/0013-7944(94)90059-0
18. Tan, Y., He, Y., Li, X., Kang, G.: A phase field model for fatigue fracture in piezoelectric solids: a residual controlled staggered scheme. Comput. Methods Appl. Mech. Eng. **399**, 115459 (2022). https://doi.org/10.1016/j.cma.2022.115459
19. Sridhar, A., Keip, M.A.: A phase-field model for anisotropic brittle fracturing of piezoelectric ceramics. Int. J. Fract. **220**, 221–242 (2019). https://doi.org/10.1007/s10704-019-00391-9
20. Tang, S., Zhang, G., Guo, T., Guo, X., Liu, W.K.: Phase field modeling of fracture in nonlinearly elastic solids via energy decomposition. Comput. Methods Appl. Mech. Eng. (2019). https://doi.org/10.1016/j.cma.2018.12.035
21. Arash, B., Exner, W., Rolfes, R.: A finite deformation phase-field fracture model for the thermo-viscoelastic analysis of polymer nanocomposites. Comput. Methods Appl. Mech. Eng. **381**, 113821 (2021). https://doi.org/10.1016/j.cma.2021.113821
22. Zuo, P., Zhao, Y.P.: Phase field modeling of lithium diffusion, finite deformation, stress evolution and crack propagation in lithium ion battery. Extreme Mech. Lett. **9**, 467–479 (2016). https://doi.org/10.1016/j.eml.2016.03.008

23. Buehler, M.J.: MechGPT, a language-based strategy for mechanics and materials modeling that connects knowledge across scales, disciplines, and modalities. Appl. Mech. Rev. (2024). https://doi.org/10.1115/1.4063843
24. Jin, H., Zhang, E., Espinosa, H.D.: Recent advances and applications of machine learning in experimental solid mechanics: a review. Appl. Mech. Rev. (2023). https://doi.org/10.1115/1.4062966
25. Dankowicz, H., Chiu, W. K. S.: Special issue of applied mechanics reviews in collaboration with the journal of electrochemical energy conversion and storage. Appl. Mech. Rev. (2023). https://doi.org/10.1115/1.4056961
26. Wang, C., Ping, X., Wang, X.: An adaptive finite element method for crack propagation based on a multifunctional super singular element. Int. J. Mech. Sci. **247**, 108191 (2023). https://doi.org/10.1016/j.ijmecsci.2023.108191
27. Miehe, C., Hofacker, M., Welschinger, F.: A phase field model for rate-independent crack propagation: robust algorithmic implementation based on operator splits. Comput. Methods Appl. Mech. Eng. **199**, 2765–2778 (2010). https://doi.org/10.1016/j.cma.2010.04.011
28. Gao, X., Jia, Y., Zhang, W., Yuan, C., Xu, J.: Mechanics-driven anode material failure in battery safety and capacity deterioration issues: a review. Appl. Mech. Rev. (2022). https://doi.org/10.1115/1.4054566
29. Liu, Z., Reinoso, J., Paggi, M.: Phase field modeling of brittle fracture in large-deformation solid shells with the efficient quasi-Newton solution and global–local approach. Comput. Methods Appl. Mech. Eng. **399**, 115410 (2022). https://doi.org/10.1016/j.cma.2022.115410
30. Francfort, G.A., Marigo, J.J.: Revisiting brittle fracture as an energy minimization problem. J. Mech. Phys. Solids **46**, 1319–1342 (1998). https://doi.org/10.1016/S0022-5096(98)00034-9
31. Bourdin, B.: Numerical implementation of the variational formulation for quasi-static brittle fracture. Interfaces Free Bound. **9**, 411–430 (2007). https://doi.org/10.4171/IFB/171
32. Wu, J.Y., Chen, W.X.: Phase-field modeling of electromechanical fracture in piezoelectric solids: analytical results and numerical simulations. Comput. Methods Appl. Mech. Eng. **387**, 114125 (2021). https://doi.org/10.1016/j.cma.2021.114125
33. Moreno-Mateos, M.A., Mehnert, M., Steinmann, P.: Electro-mechanical actuation modulates fracture performance of soft dielectric elastomers. Int. J. Eng. Sci. **195**, 104008 (2024). https://doi.org/10.1016/j.ijengsci.2023.104008
34. Russ, J., Slesarenko, V., Rudykh, S., Waisman, H.: Rupture of 3D-printed hyperelastic composites: experiments and phase field fracture modeling. J. Mech. Phys. Solids **140**, 103941 (2020). https://doi.org/10.1016/j.jmps.2020.103941
35. Shahba, A., Ghosh, S.: Coupled phase field finite element model for crack propagation in elastic polycrystalline microstructures. Int. J. Fract. **219**, 31–64 (2019). https://doi.org/10.1007/s10704-019-00378-6
36. Tan, Y., He, Y., Li, X.: Phase field fracture modeling of transversely isotropic piezoelectric material with anisotropic fracture toughness. Int. J. Solids Struct. (2022). https://doi.org/10.1016/j.ijsolstr.2022.111615
37. Park, S., Sun, C.T.: Fracture criteria for piezoelectric ceramics. J. Am. Ceram. Soc. **78**, 1475–1480 (1995). https://doi.org/10.1111/j.1151-2916.1995.tb08840.x
38. Wu, J.Y., Huang, Y., Nguyen, V.P.: On the BFGS monolithic algorithm for the unified phase field damage theory. Comput. Methods Appl. Mech. Eng. (2020). https://doi.org/10.1016/j.cma.2019.112704
39. Molnár, G., Gravouil, A.: 2D and 3D Abaqus implementation of a robust staggered phase-field solution for modeling brittle fracture. Finite Elem. Anal. Des. **130**, 27–38 (2017). https://doi.org/10.1016/j.finel.2017.03.002
40. Amor, H., Marigo, J.J., Maurini, C.: Regularized formulation of the variational brittle fracture with unilateral contact: numerical experiments. J. Mech. Phys. Solids **57**, 1209–1229 (2009). https://doi.org/10.1016/j.jmps.2009.04.011
41. Ambati, M., Gerasimov, T., De Lorenzis, L.: A review on phase-field models of brittle fracture and a new fast hybrid formulation. Comput. Mech. **55**, 383–405 (2015). https://doi.org/10.1007/s00466-014-1109-y
42. Seleš, K., Lesičar, T., Tonković, Z., Sorić, J.: A residual control staggered solution scheme for the phase-field modeling of brittle fracture. Eng. Fract. Mech. **205**, 370–386 (2019). https://doi.org/10.1016/j.engfracmech.2018.09.027